

Data Assimilation with Machine Learning Surrogate Models: A Case Study with FourCastNet

Melissa Adrian^{*1}, Daniel Sanz-Alonso¹, and Rebecca Willett^{1,2}

¹Department of Statistics, The University of Chicago, Chicago, IL 60637, USA

²Department of Computer Science, The University of Chicago, Chicago, IL 60637, USA

Abstract

Modern data-driven surrogate models for weather forecasting provide accurate short-term predictions but inaccurate and nonphysical long-term forecasts. This paper investigates online weather prediction using machine learning surrogates supplemented with partial and noisy observations. We empirically demonstrate and theoretically justify that, despite the long-time instability of the surrogates and the sparsity of the observations, filtering estimates can remain accurate in the long-time horizon. As a case study, we integrate FourCastNet, a state-of-the-art weather surrogate model, within a variational data assimilation framework using partial, noisy ERA5 data. Our results show that filtering estimates remain accurate over a year-long assimilation window and provide effective initial conditions for forecasting tasks, including extreme event prediction.

1 Introduction

Numerical weather prediction (NWP) at an operational scale relies on large-scale systems of partial differential equations to model atmospheric dynamics. However, these physics-based models are computationally expensive to simulate, particularly when operating at a high resolution. This computational burden plagues both weather and climate models alike [Tollefson, 2023], leading research focus to shift towards cheaper alternatives: data-driven machine learning surrogate models for weather forecasting.

Weather surrogate models have been analyzed and evaluated extensively using high-resolution accurate datasets, usually ERA5 reanalysis data [Hersbach et al., 2020]. However, in practical weather forecasting settings, we must provide high-fidelity forecasts given only sparse observations, often contaminated with measurement errors. Because major advances in high-resolution data-driven global weather modeling have only been made in the past few years, substantial work has yet to be done to analyze its utility in settings of operational interest, including both data assimilation and forecasting with these sparse and noisy observations.

Data assimilation is an operational task with a long history in weather forecasting, rooted in seminal works, such as Richardson [1922], Kalman [1960], and Gandin [1966]. Preliminary data assimilation methods were developed specifically for the vast problem that characterizes weather settings: inferring a high-resolution representation of the atmosphere with only (1) sparse, noisy measurements throughout the globe and (2) a time evolution mapping of atmospheric states. Data assimilation produces high-dimensional representations, also referred to as analyses, which provide a detailed view of historical global weather patterns. These analyses can be used for numerous purposes, most notably to initialize forecasts based on current and historical observations. However, producing analyses using physics-based NWP models is computationally expensive, especially for long time horizons. Consequently, cheap-to-evaluate surrogate weather models have enormous potential to expedite this data assimilation process.

The potential of weather surrogate models to accelerate extreme event prediction has recently received attention at the government level, with an April 2024 U.S. Executive Office report calling attention to its potential widespread operational use [The President’s Council of Advisors on Science and Technology, 2024]. This report stated that in the U.S. in 2023 alone, the economic damage due to extreme weather events totalled to \$92.9 billion from 28 weather disasters, and the frequency of these extreme events is expected to continue to increase in the coming years [The President’s Council of Advisors on Science and Technology, 2024]. This staggering economic loss and the projected increased frequency in weather disasters point to the escalating

*Corresponding author: maadrian@uchicago.edu

need for real-time, accurate weather forecasting. Surrogate weather models allow for real-time forecasting and uncertainty quantification given an accurate estimate of the initial or current weather state, which could be especially impactful for time-sensitive extreme events like hurricanes, typhoons, cyclones, etc. In the event of extreme weather, it is paramount to produce, in real time, accurate estimates of the state of the weather to initialize forecasts, which can be accomplished via data assimilation. Moreover, quickly computing large ensembles of forecasts using these weather surrogates allows for a timely characterization of the distribution of potential future outcomes. Speed, accuracy, and uncertainty quantification are crucial to gauge the severity and likelihood of these potential outcomes and subsequently inform timely decisions regarding public safety. In our evaluation tasks for extreme events, we especially inspect the predicted severity of these events compared to the actual severity. As a case study, we compute forecasts of Typhoon Mawar in 2023 and assess the U- and V-component wind speed at 10 meters (10m) above Earth’s surface, the mean sea level pressure, and the location of the typhoon’s eye to characterize the quality of forecasts given various types of initializations, including the data assimilation analyses we produce.

In our work, we aim to assess the utility of weather surrogate models, particularly a state-of-the-art weather surrogate model, FourCastNet [Pathak et al., 2022], in the three main tasks of operational interest: (1) estimation of the high-dimensional weather state from low-resolution observations via a variational data assimilation framework, (2) multi-step-ahead forecasting using these estimates, and as a more focused forecasting task, (3) extreme event prediction using these estimates. Our high-dimensional state consists of 20 atmospheric features at various pressure levels in the atmosphere at a global 0.25° resolution, corresponding to a 720×1440 grid. We utilize (1) FourCastNet as our weather model, (2) low-resolution, noisy ERA5 reanalysis data [Hersbach et al., 2020] as a proxy for real observations, and (3) a 3DVar variational data assimilation algorithm [Lorenc et al., 2000] to combine forecasts and observations. We demonstrate that pairing FourCastNet within 3DVar to assimilate low-resolution, noisy observational data can produce visually realistic weather patterns while maintaining a stable reconstruction error over a long time horizon, and we provide a theoretical justification for this result. Additionally, we show that these 3DVar analyses can serve as effective initial conditions for forecasting tasks, even in our extreme event case study.

2 Contributions

This work provides new empirical and theoretical evidence that data-driven surrogate models for weather forecasting can be successful in data assimilation tasks. We illustrate the potential of purely data-driven, global weather data assimilation using a current state-of-the-art weather surrogate model, FourCastNet, and low-resolution, noisy data. Our assimilation is based on a simple 3DVar filter that can be run with a single 80GB NVIDIA A100 GPU. The main contributions of this paper are to:

1. Empirically show the accuracy of 3DVar filtering with FourCastNet over a year-long assimilation window given a sufficiently rich set of low-resolution, noisy observations.
2. Rigorously prove long-time assimilation accuracy of 3DVar with a short-time accurate surrogate forecast model and a sufficiently rich set of partial, noisy observations.
3. Demonstrate that filtering estimates provide successful initial conditions for forecasting tasks, including extreme event prediction.

3 Related work

In recent years, there have been substantial advances in machine learning to create surrogates of numerical weather models in order to produce predictions at a fraction of the cost while maintaining short-term accuracy. Notable global data-driven weather models include FourCastNet [Pathak et al., 2022], Pangu [Bi et al., 2023], GraphCast [Lam et al., 2023], a graph-based weather model from [Keisler, 2022], FengWu [Chen et al., 2023a], and FuXi [Chen et al., 2023b]. In this work, we focus on evaluating FourCastNet as a case study.

In addition to training high-fidelity data-driven weather models, machine learning for weather and climate applications is rapidly advancing in many other directions. Krasnopolsky [2023] provides a current overview of advances in machine learning for data assimilation, modeling physics, and post-processing for weather and climate systems. Additionally, Cheng et al. [2023], Chen [2023, Chapter 10], and Bocquet [2023] survey current approaches to combine machine learning with data assimilation, including the use of surrogate forecast models that is the focus of our work.

Data-driven weather forecasting in data assimilation Some recent works have explored replacing numerical weather prediction models with data-driven prediction models trained on smaller-scale datasets. For instance, Chattopadhyay et al. [2022] develops a data-driven weather prediction architecture for a 5.625° resolution representation of global geopotential at 500 hPa, corresponding to a 32×64 latitude/longitude grid. This work shows success in providing analyses that accurately estimate the ground truth using a sigma-point ensemble Kalman filter [Tang et al., 2014] paired with their novel architecture. Another example is Maulik et al. [2022], which builds a surrogate model of geopotential height at 500 hPa over North America. Maulik et al. [2022] shows that using their trained surrogate model within a 4DVar algorithm [Le Dimet and Nouailler, 1986] produces analyses that, when used as initial conditions for forecasting tasks, outperform forecasts that are initialized based on climatology.

The successes on smaller scale data point to potential success for larger scale integration of weather surrogates in data assimilation tasks. Huang et al. [2024] and Xiao et al. [2023] are among the first works to combine data assimilation and a state-of-the-art weather surrogate at a high dimensional scale. Huang et al. [2024] performs a data assimilation task at an operational scale by reconstructing 24 atmospheric features at a 0.25° resolution (721×1440 grid) with the data-driven weather surrogate GraphCast [Lam et al., 2023]. In addition, the authors formulate a novel alternative to traditional data assimilation tasks through the use of a learnable diffusion model. Huang et al. [2024], however, focuses on short assimilation horizons and one-step-ahead forecasting in its experiments and utilizes a diffusion-based architecture, which may suffer from inefficiencies in sample generation speed. Addressing this generation speed issue is an area of active research [Chen et al., 2024]. In our work, we expand upon evaluation tasks to assess the quality of longer forecasts using data assimilation analyses in a computationally efficient manner.

Xiao et al. [2023] combines FenguWu [Chen et al., 2023a] within a 4DVar assimilation scheme to estimate a latent representation consisting of 69 atmospheric features at a roughly 1.41° spatial resolution, corresponding to a 128×256 grid. This work assimilates observations that were created from ERA5 data with randomly applied masks, leading to 15% of locations being observed [Xiao et al., 2023]. Similarly to the results we present in this paper, Xiao et al. [2023] shows stable analysis errors across the span of a year. Our work demonstrates similar error stability for a higher dimensional representation of global weather patterns (0.25° resolution) using lower resolution observations (observing at most 1.5% of locations) compared to Xiao et al. [2023] for observations acquired at fixed spatial locations.

Stability theory of 3DVar accuracy. Many works have analyzed long-term stability and accuracy of nonlinear filtering algorithms [Crisan and Rozovskii, 2011] and data assimilation techniques [Kalnay, 2003] that employ the true model for the dynamics. In particular, a large body of work exemplified by Hayden et al. [2011]; Sanz-Alonso and Stuart [2015]; Law et al. [2016] has established long-time filter accuracy for a wide class of atmospheric models building on the rich theory of synchronization in chaotic dynamical systems [Pecora and Carroll, 1990]. The key idea is that, while for chaotic systems small errors in state estimation are typically exponentially amplified by the dynamics, this growth of errors can be tamed if sufficiently rich observations of the state are assimilated in an online fashion.

Our main theoretical result, Theorem 1, establishes long-time accuracy for a 3DVar filtering algorithm that utilizes a surrogate model of the true dynamics. We assume only that (1) the surrogate model is accurate over one assimilation cycle and (2) the observations are sufficiently rich to achieve long-time filter accuracy with a 3DVar algorithm that employs the true dynamics model. Our result is hence similar to Moodey et al. [2013], which also establishes accuracy under model error, but in contrast to Moodey et al. [2013] we place no assumptions on the surrogate model other than short-time accuracy, thus making our theory more directly relevant to the context of complex machine learning surrogates for weather forecasting.

4 Data description

ERA5 is a reanalysis dataset that provides hourly atmosphere, land, and ocean feature estimates produced by the variational data assimilation method 4DVar [Rawlins et al., 2007] at a resolution of 0.25° using observational weather data from 1979 to present day [Hersbach et al., 2020]. Data was pulled from the Copernicus Climate Data Store, Sabater [2019] for land features, and Hersbach et al. [2023] for pressure level features. We retain only a subset of the atmospheric features in ERA5, specifically total column water vapor (TCWV), geopotential at 50, 500, 850, and 1000 hPa, U-component wind speed at 10 meters from the surface and at 500, 850, and 1000 hPa, V-component wind speed at 10 meters from the surface and at 500, 850, and 1000 hPa, relative humidity at 500 and 850 hPa, temperature at 2 meters from the surface and at 500 and 850 hPa, surface pressure (sp), and mean sea level pressure (mslp). Consequently, we retained all the features that FourCastNet was trained to

k	Resolution	Latitude/longitude grid size	Distance between observations along the equator	% of latent states observed
8	2°	90×180	222 km	1.56%
10	2.5°	72×144	278 km	1.00%
18	4.5°	40×80	500 km	0.31%
20	5°	36×72	556 km	0.25%

Table 1: Table describing the observational dataset resolution with corresponding distances between observations along the equator and percentage of the latent states observed for each dataset. In each of these datasets, we observe all 20 atmospheric features for every k -th latent location in both the latitude and longitude directions. As reference, the latent states have a resolution of 0.25° , which corresponds to a distance of 28 km between latent states along the equator and a latitude/longitude grid size of 720×1440 .

predict. Additionally, we standardized the ERA5 dataset using the same global feature means and standard deviations that were used in training FourCastNet.

As described next, for our assimilation and forecasting tasks, the true latent states represent high-resolution ERA5 data across 2023, from which we create low-resolution noisy observations. We emphasize that our chosen time range, ERA5 data for 2023, is disjoint from the time range that FourCastNet was trained and tuned on, ERA5 data from 1979 to 2017 [Pathak et al., 2022].

True latent states $\{x_t^{\text{true}}\}_{t=0}^T$. The true state $x_t^{\text{true}} \in \mathbb{R}^{d_x}$ at time t represents 20 ERA5 atmospheric features at a 0.25° resolution, which results in a state dimension $d_x = 20 \times 720 \times 1440 = 20,736,000$ at one time point. This state is partially observed every 6 hours for the entirety of 2023, so we consider $T = 1460$ time points (4 observations/day $\times 365$ days). Thus, $t = 0$ corresponds to January 1, 2023 at 00:00 UTC, and $t = T$ corresponds to December 31, 2023 at 18:00 UTC.

Observations y_t . The observations y_t represent data collected at a lower spatial resolution than the true state x_t^{true} . We seek to estimate the high-resolution weather state from these low-resolution observations. In our experiments, we generate low-resolution y_t from x_t^{true} to explore the efficacy of the proposed approach for data assimilation using weather surrogate models. Specifically, we generate y_t using coarse measurements of the 20 ERA5 atmospheric features. To generate these observations, we systematically thin out the ERA5 latitude/longitude grid to retain all atmospheric features at every k -th coordinate in the latitude and longitude directions, where we vary k in our assimilation experiments in Section 6.1. We additionally add $\mathcal{N}(0, R)$ distributed noise to this ground truth coarsened ERA5 data to model measurement error, where $R = 0.0001I_{d_y}$ and \mathcal{N} refers to a normal distribution. For a given k , our observations are $y_t \in \mathbb{R}^{d_y}$, where $d_y = 720/k \times 1440/k \times 20 = 20,736,000/k^2$. We give an interpretation of our choices of k in Table 1. As an illustrative example, Appendix A provides a visualization of ground truth ERA5 data in its native 0.25° resolution compared to the 4.5° observations for relative humidity at 500 hPa.

We note that when we discuss observations in a generic data assimilation setting, we describe them as sparse and noisy, while in our experiments, we describe observations as low-resolution and noisy. This difference in language is to emphasize that in generic assimilation settings with observations taken from real sensors, satellites, etc., these observations can be non-uniformly spaced, with the spacing being different for different weather features. In our experimental settings, however, the observations follow a regular, coarsened grid structure.

5 Methodology

5.1 Setting

Our goal is to estimate a high-dimensional latent state $\{x_t^{\text{true}}\}_{t \geq 1}$ given observations $\{y_t\}_{t \geq 0}$, which are derived from the following setting:

$$\begin{aligned} x_t^{\text{true}} &= \mathcal{F}(x_{t-1}^{\text{true}}), \\ y_t &= Hx_t^{\text{true}} + \eta_t, \quad \eta_t \sim \mathcal{N}(0, R), \end{aligned} \tag{1}$$

where \mathcal{F} is the true dynamics governing the evolution of the state, H is a linear observation operator, and R is a known measurement error covariance matrix. We are interested in online estimation, so that at each time t our

estimate of the state x_t^{true} should only depend on the observations $\{y_0, \dots, y_t\}$ available at time t . Again, our goal is to reconstruct these high-dimensional states in 6-hourly increments across the year 2023 for $t = 1, \dots, T$, where $T = 1460$. We next describe the specific problem settings for our numerical results.

Observation operator H . The observation operator $H \in \{0, 1\}^{d_y \times d_x}$ is a subset of the rows of the identity matrix, with the remaining rows indicating wherever a latent dimension is observed. Our H is independent of time, meaning that we observe the same subset of locations throughout the entire assimilation horizon.

5.2 3DVar

We utilize the 3DVar filtering algorithm [Lorenc et al., 2000] to sequentially estimate the true high-dimensional states $\{x_t^{\text{true}}\}_{t \geq 1}$. At each time $t \geq 1$, the state filtering estimate x_{t-1}^s is projected forward in time using the surrogate model dynamics in a forecast step (2), and this forecast is corrected using the new observation y_t in an analysis step (3):

$$\text{(forecast)} \quad \hat{x}_t = \mathcal{F}_s(x_{t-1}^s), \quad (2)$$

$$\text{(analysis)} \quad x_t^s = \hat{x}_t + CH^T(HCH^T + R)^{-1}(y_t - H\hat{x}_t). \quad (3)$$

For brevity and later reference, we can write (2) and (3) as

$$x_t^s = (I - KH)\mathcal{F}_s(x_{t-1}^s) + Ky_t, \quad t \geq 1 \quad (4)$$

where $K = CH^T(HCH^T + R)^{-1}$. Here, \mathcal{F}_s represents a surrogate forecast model for the dynamics. In our experimental results, the observation operator H is described in Section 5.1, and the time horizon T , observations y_t for $1 \leq t \leq T$, and observation error covariance R are described in Section 4. We next specify the initialization x_0 , surrogate dynamics map \mathcal{F}_s , and background covariance C .

3DVar initialization x_0 . We define our 3DVar initialization x_0 to be interpolated and standardized y_0 data. These low-resolution observations with $\mathcal{N}(0, R)$ additive noise are interpolated to a 720×1440 grid, or a 0.25° resolution, for 20 atmospheric features on January 1, 2023 at 00:00 UTC. The interpolation first uses the nearest neighbor algorithm, then smoothed using a 2D convolution with weight matrix $W^{(k)} \in \mathbb{R}^{k \times k}$, where

$$W_{i,j}^{(k)} = \frac{\tilde{w}_{i,j}}{\sum_i \sum_j \tilde{w}_{i,j}}, \quad (5)$$

$$\tilde{w}_{i,j} = \exp \left\{ \frac{-(i - m_i)^2 - (j - m_j)^2}{2\sigma^2} \right\},$$

$$i = 1, \dots, k, \quad j = 1, \dots, k,$$

$$m_i = \lfloor k/2 \rfloor, \quad \text{and } m_j = \lfloor k/2 \rfloor,$$

and stride (1, 1) for each of the 20 features. For each observation resolution, $\sigma^2 = 8$.

Surrogate dynamics map \mathcal{F}_s . The surrogate weather model utilized throughout our assimilation experiments takes the form

$$\mathcal{F}_s = S \circ \mathcal{F}_{\text{FCN}}, \quad (6)$$

where \mathcal{F}_{FCN} represents FourCastNet [Pathak et al., 2022] and S is a smoothing convolution used to enhance filter stability.

The Fourier Forecasting Neural Network (FourCastNet) [Pathak et al., 2022] provides global weather predictions at 0.25° resolution for short to mid-range time horizons across 20 atmospheric features across various layers of the atmosphere. Since FourCastNet combines transformers [Dosovitskiy et al., 2021] and adaptive Fourier Neural Operators [Guibas et al., 2022], evaluating FourCastNet is substantially faster than simulating physics-based weather models, allowing for extremely quick predictions and cheap downstream analysis.

To enhance filter stability, we utilize a smoothing operator S defined as a 2D convolution with weight matrix $W^{(4)} \in \mathbb{R}^{4 \times 4}$ as in equation (5), and stride (1, 1) for each of the 20 atmospheric features. We set $\sigma^2 = 8$. This smoothing operation attempts to control instabilities in the dynamics model.

Background error covariance C . We specify that $C = qBB^T$, where B is a matrix representing 2D convolution with weight matrix $W^{(k)} \in \mathbb{R}^{k \times k}$ defined in equation (5), and stride (1,1) for each of the 20 atmospheric features. In our experiments, we vary the size of the convolutional kernel across observational data resolutions according to k . In our experiments, we choose $q = 0.5 / \sum_{i=1}^k \sum_{j=1}^k \{W_{i,j}^{(k)}\}^2$. The constant 0.5 was heuristically chosen to be a similar magnitude to one-step-ahead forecasting errors for \mathcal{F}_s in the standardized space. For each $W^{(k)}$, we set $\sigma^2 = 8$. With our choices of C and H for each observation resolution, the matrix $(HCH^T + R)^{-1}$ in the analysis step in (3) is diagonal, which results in substantial computational savings. This C matrix was constructed mainly to maximize computational efficiency and may lead to some physically unrealistic analyses that cause FourCastNet predictions to degrade. Future work can include a more sophisticated construction of this C , for example, via the widely adopted National Meteorological Center’s method described in Parrish and Derber [1992].

5.3 Theoretical long-time accuracy of 3DVar

We are interested in applications where evaluating the ground truth dynamics map \mathcal{F} is unfeasible or computationally expensive, such as a NWP model, but we have a surrogate model \mathcal{F}_s that can be cheaply evaluated, such as FourCastNet as used in (6). We prove long-time accuracy for a filtering algorithm that uses the surrogate dynamics \mathcal{F}_s rather than the true dynamics \mathcal{F} in a 3DVar data assimilation task. The result we show relies on (1) standard observability conditions on the true dynamics \mathcal{F} and observation model H and (2) accuracy of the surrogate model \mathcal{F}_s in the part of the state-space that is not informed by the observations. Here, \mathcal{F} and \mathcal{F}_s represent the flow between observation time points, i.e., 6-hour forecasts. Therefore, it is reasonable to assume that \mathcal{F}_s is a good approximation of \mathcal{F} since surrogate weather models provide accurate short-term predictions.

Formally, the goal of 3DVar is to estimate a signal $\{x_t^{\text{true}}\}_{t \geq 1}$ given observations $\{y_t\}_{t \geq 1}$ in the setting in (1). We want to study the filter accuracy for a surrogate 3DVar filter of the data assimilation scheme defined in (2) and (3).

Assumption 1. *Suppose the observations we collect are noisy, potentially sparse, unbiased measurements of the ground truth state. More precisely, suppose the data y_t in the surrogate algorithm (4) is found from observing a true signal x_t^{true} given by*

$$\begin{aligned} x_t^{\text{true}} &= \mathcal{F}(x_{t-1}^{\text{true}}), \\ y_t &= Hx_t^{\text{true}} + \gamma\eta_t, \end{aligned}$$

for $t \geq 1$ and where η_t are i.i.d. and $\mathbb{E}\|\eta_t\| < A$ for some constant $A > 0$.

Theorem 1. *Suppose Assumption 1 holds. Additionally suppose that the Kalman gain matrix K in (4) satisfies that, for some constant $\lambda \in (0, 1)$,*

$$\|(I - KH)D\mathcal{F}(x)\| \leq \lambda \quad \forall x \in \mathbb{R}^{d_x}, \quad (7)$$

where $D\mathcal{F}$ denotes the Jacobian matrix of \mathcal{F} . Suppose further that

$$\|(I - KH)(\mathcal{F}_s(x) - \mathcal{F}(x))\| \leq \varepsilon \quad \forall x \in \mathbb{R}^{d_x}. \quad (8)$$

Then, there exists a constant $c > 0$ independent of γ , λ , and ε such that the surrogate 3DVar algorithm satisfies

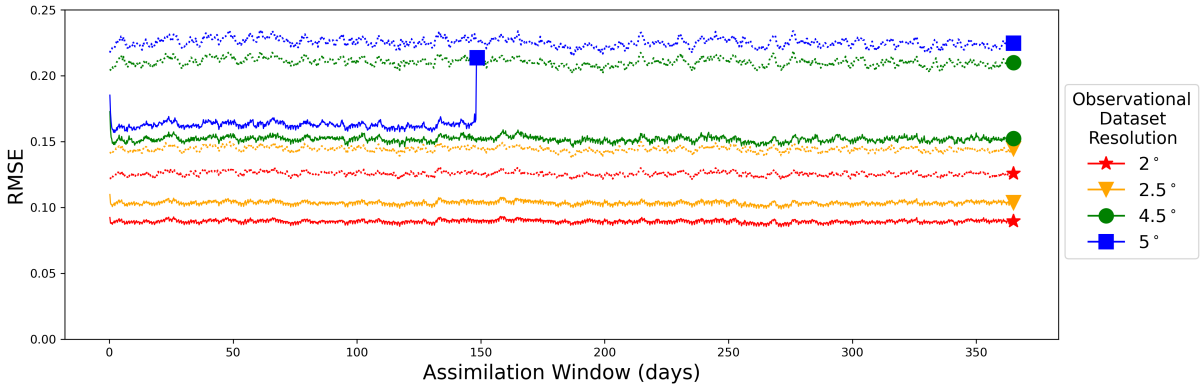
$$\limsup_{t \rightarrow \infty} \mathbb{E}\|x_t^s - x_t^{\text{true}}\| \leq c \left(\frac{\gamma + \varepsilon}{1 - \lambda} \right). \quad (9)$$

We include a proof of Theorem 1 in Appendix B.

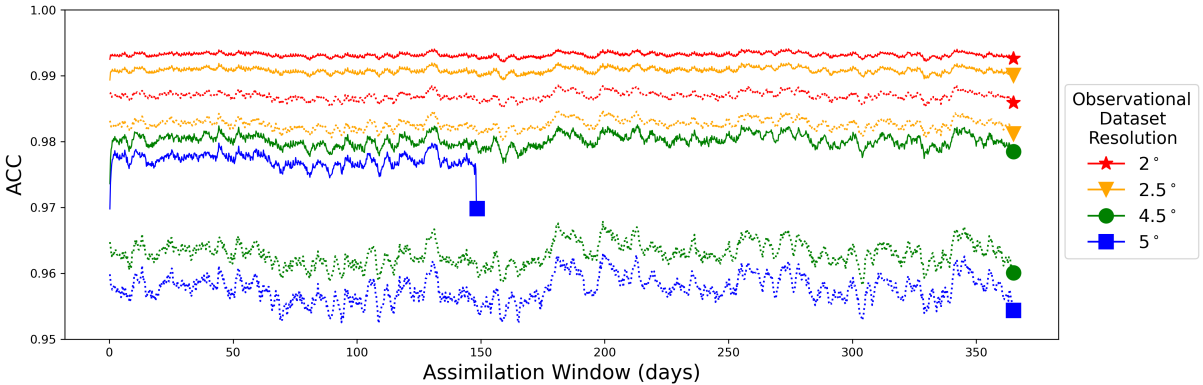
A key emphasis on our theoretical result is that we only assume that the surrogate model is accurate for short-term horizons, yet we can still obtain long-term analysis stability using it as a dynamics model by leveraging observations $\{y_t\}_{t \geq 1}$. To summarize, our theory rigorously shows that if we have long-term filter accuracy with the true dynamics model \mathcal{F} and a surrogate model \mathcal{F}_s that provides accurate short-term forecasts, we can achieve long-term filter accuracy with the surrogate dynamics.

6 Results

Our results evaluate the empirical long-term assimilation stability of 3DVar with our chosen surrogate \mathcal{F}_s in (6) and with varying resolutions of noisy ERA5 data as observations. We evaluate the forecasting performance using



(a) RMSE across a year-long assimilation window for different observational dataset resolutions, evaluated using standardized 2023 ERA5 data.



(b) ACC across a year-long assimilation window for different observational dataset resolutions, evaluated using standardized 2023 ERA5 data.

Figure 1: The dotted lines in both (a) and (b) correspond to metrics for interpolated noisy observations at each time point, and solid lines correspond to metrics for the 3DVar analyses. These metrics are computed using standardized ERA5 data and standardized predictions, and the results are reported as average standardized errors across our 20 atmospheric features. These results show that our 3DVar analyses yield lower RMSE and higher ACC metrics across a year compared to interpolating raw observations. Furthermore, our 3DVar analyses using low-resolution observations achieve stable metrics up to a 5° resolution. At the 5° observation resolution, the analysis can be unstable, and we display metrics only up to the time that the instability was detected.

our 3DVar analyses as initial conditions and compare against a more naive approach of forecasting using only the interpolated observations as initial conditions. These interpolated observations are constructed in the same way as our 3DVar initialization x_0 in Section 5.2 for each $\{y_t\}_{t=1}^T$. The performance of these two approaches is averaged across 20 standardized atmospheric features and compared to a so-called “gold standard” where we compute forecasting metrics using ground truth ERA5 initializations. The comparison to this gold standard is included to contextualize how well we could expect to perform in these forecasting tasks in an ideal setting: ground truth information upon initialization. To further explore the task of forecasting, we assess the forecasting performance of an extreme event, Category 5-equivalent super typhoon, Typhoon Mawar in 2023.

We evaluate each of our tasks on 2023 ERA5 reanalysis data using the metrics latitude-weighted root-mean-square-error (RMSE) and latitude-weighted anomaly correlation coefficient (ACC). We provide a detailed explanation of our error metrics in Appendix C.

6.1 Empirical stability of 3DVar paired with FourCastNet for various observation sizes

We considered four observation resolutions for our assimilation tasks, ranging considerably in sizes. Specifically, our four datasets contain observations of all 20 atmospheric features at every 2°, 2.5°, 4.5°, and 5° in the latitude and longitude directions, with additive $\mathcal{N}(0, R)$ noise. Table 1 provides further details with characteristics about these datasets. We again emphasize that the observation locations remain static throughout our assimilation.

In Figures 1a and 1b, we show the filtering RMSEs and ACCs of our 3DVar implementation for various

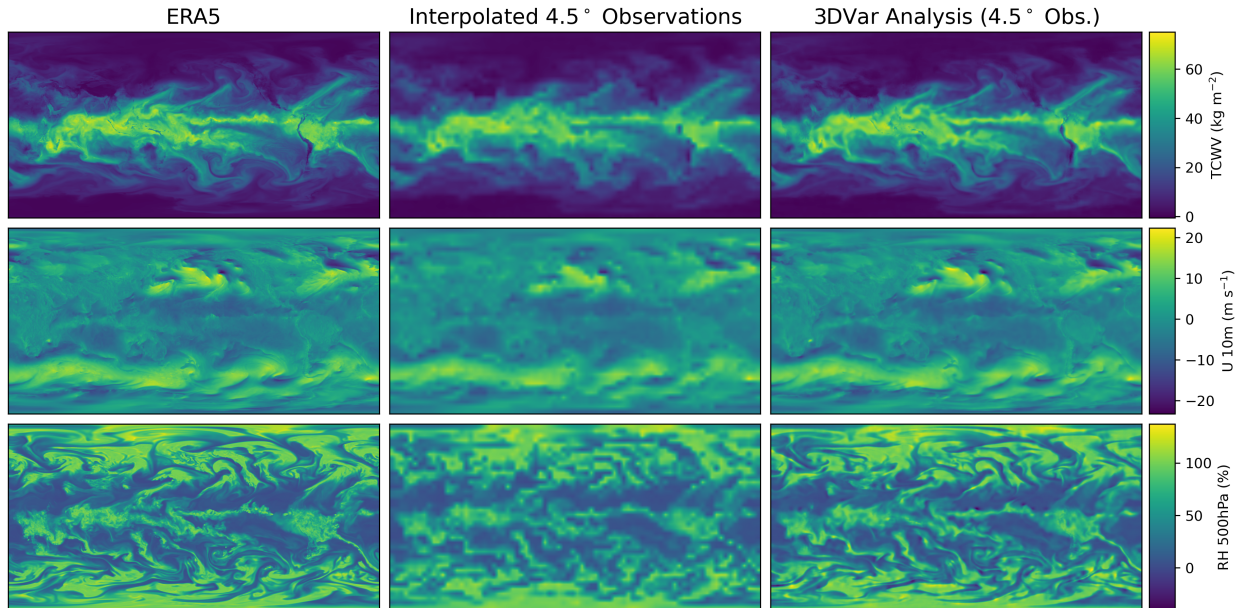


Figure 2: Visualization of the ground truth ERA5 data, interpolated 4.5° ERA5 observations with standardized $N(0, 0.0001I_{d_y})$ distributed additive errors, and our 3DVar analysis using this observational data and FourCastNet for the atmospheric features total column water vapor (TCWV), U-component wind speed at 10m above the surface (U 10m), and relative humidity at 500 hPa (RH 500hPa) at the end of our assimilation horizon, December 31, 2023 at 18:00 UTC.

observation resolutions computed based on ground truth ERA5 data across 2023. As a baseline for comparison, we compute the error for interpolating our low-resolution, noisy observations based on the ground truth ERA5 data. A sufficiently well-calibrated 3DVar implementation would provide better performance compared to this naive baseline, which is the case with our 3DVar analyses.

Comparing our 3DVar analysis RMSEs and ACCs (solid lines) against our naive observation interpolation baseline (dotted lines) for each observation resolution, we notice a consistent and substantial gap in performance in favor of our 3DVar analysis. To qualitatively visualize this gap in performance, we show in Figure 2 the ground truth ERA5, interpolated 4.5° observations, and our 3DVar analysis with these 4.5° observations at the end of our assimilation window, corresponding to December 31, 2023 18:00 UTC. The interpolated observations clearly show lack of detail and are overly smooth, which is particularly noticeable in features with sharp gradients throughout the globe, such as relative humidity at 500 hPa. In contrast, our 3DVar analysis using FourCastNet and these 4.5° observations show higher quality detail with an appropriate smoothness and detail given the feature. The presence of these details can be attributed to smaller-scale information encoded in the FourCastNet forward pass. To further emphasize this performance gap, we include similar visualizations comparing the ground truth ERA5 data, interpolated 4.5° observations, and our 3DVar analyses with these 4.5° observations for all 20 atmospheric features at the end of our year-long assimilation in Appendix D.

We note that the assimilation 5° observations in Figures 1a and 1b exhibited filter divergence after assimilating about 150 days worth of observational data, despite the smoothing operation we employed in (2) for filter stability. Since a 5° is a very sparse dataset, corresponding to observing only 0.25% of the latent states, and additionally given the simplifying assumptions underlying our construction of C in (3), filter divergence is unsurprising. In the context of our stability theory, for this choice of K that depends on C , the upper-bound λ in (7) is large. We speculate that with more sophisticated assumptions on the latent state covariance C , analysis stability for this time horizon may be achievable.

6.2 Forecasting accuracy given various initializations

We consider the task of h -step ahead forecasting given four different types of initializations. More specifically, as shown in Figure 3 we forecast with (a) interpolated 4.5° observations, (b) ground truth ERA5 data (as a gold standard), (c) 3DVar analyses using these 4.5° observations, and (d) climatology as initializations. Initializations (a) and (d) serve as baselines that a well-calibrated 3DVar analysis would outperform in terms of forecasting error metrics, and (b) serves as a point of comparison in order to tangibly assess the effect of the estimations in (a), (c), and (d). We report metrics in terms of standardized predictions compared to standardized ground truth

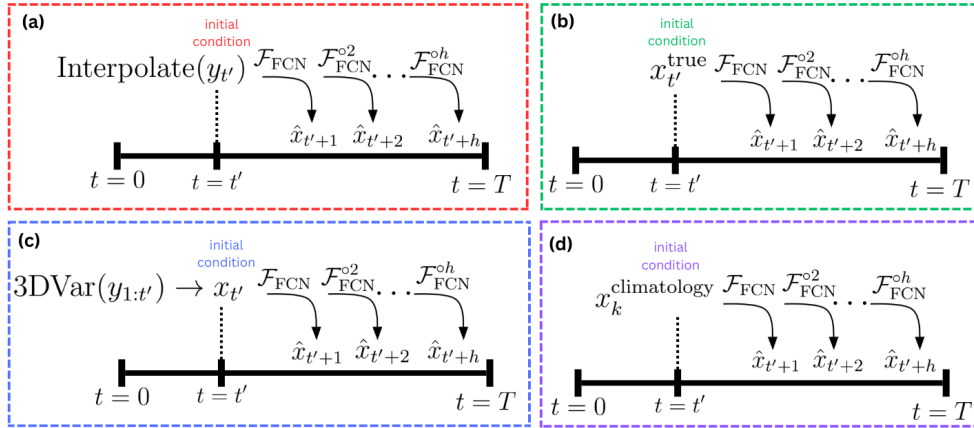


Figure 3: Visualization of various forecasting initializations for the task of h -step-ahead forecasting. An initialization at time t' is used to autoregressively compute forecasts up to h time steps ahead using \mathcal{F}_{FCN} , FourCastNet. The initialization time t' varies between $1 \leq t' \leq T - h$ for all tasks (a)-(d). We consider forecasting using (a) interpolated observations, (b) true ERA5 data (unavailable in practice, serving here as a gold standard), (c) 3DVar analyses, and (d) climatology as initializations. Additionally, $t = 0$ corresponds to January 1, 2023 at 00:00 UTC, and $t = T$ corresponds to December 31, 2023 at 18:00 UTC.

ERA5 data. We utilize a climatology dataset, which corresponds to the mean value for each spatial location and feature from the years 1979 to 2015 in the ERA5 dataset.

Figure 4 shows the RMSEs and ACCs across a 5 day forecasting horizon, averaged across different initial time points within 2023. We note that both the interpolated observations and our 3DVar analyses substantially outperform climatology as an initial condition for our forecasting tasks. This result is to be expected, given that climatology reflects historical averages rather than real-time information that substantially impacts the short-term weather dynamics that we consider. We additionally note that our 3DVar analysis shows a noticeable performance improvement compared to the interpolated observations, particularly in short-term forecasts. The difference in performance is most noticeable within the first roughly 48 hours of the forecast initialization, after which differences in the average forecasting performance become less noticeable.

In producing Figure 4, we encountered two out of 1432 time points where our 3DVar analyses with 4.5° observations, when used as initial conditions for FourCastNet, resulted in degraded forecasts after a roughly 2 day forecasting horizon. These degraded forecasts are characterized by large, physically unrealistic predicted values originating from diverging forecasts originating at a particular location on the globe. The two time points corresponded to an extreme event, specifically Typhoon Khanun, and the forecasting errors autoregressively accumulated in the region of this typhoon. Such catastrophic forecast errors were not seen in the forecasts using climatology, interpolated 4.5° observations, or ground truth ERA5 data. Because we did not see the same catastrophic forecasting divergence in our 3DVar analyses with 2° and 2.5° observation resolutions, we hypothesize that our 4.5° 3DVar analyses at these two time points do not have enough data near the typhoon to adequately estimate a physically realistic initial condition given the construction of our 3DVar algorithm, leading to downstream forecasting divergence.

6.3 Extreme event: Typhoon Mawar, 2023

Despite the substantial computational advantage data-driven forecasting models provide compared to physics-based models to create forecasting initial conditions, maintaining a satisfactory level of accuracy in forecasts produced from these initial conditions is equally important, especially when considering the substantial impacts that inaccurate forecasts can have on communities during times of extreme events. For example, under-predicting the severity of an extreme event can lead to decision-makers to inadequately inform the public about recommended safety measures. These forecasts need to be accurate enough to properly inform recommendations of disaster mitigation measures, and also computationally cheap enough to be produced in a timely manner.

For these reasons, we narrow our attention in our forecasting evaluation to consider extreme events, and we choose Typhoon Mawar in 2023 as a case study. On May 24, 2023, Typhoon Mawar passed just north of Guam as a category 4-equivalent typhoon, leaving a large portion of the island of 150,000 inhabitants without power [National Environmental Satellite, Data, and Information Service, NOAA, 2023]. Soon after, the typhoon achieved category 5-equivalent status on the Saffir-Simpson Hurricane Wind Scale, with maximum wind speeds recorded on May 26, 2023 [National Environmental Satellite, Data, and Information Service, NOAA, 2023].

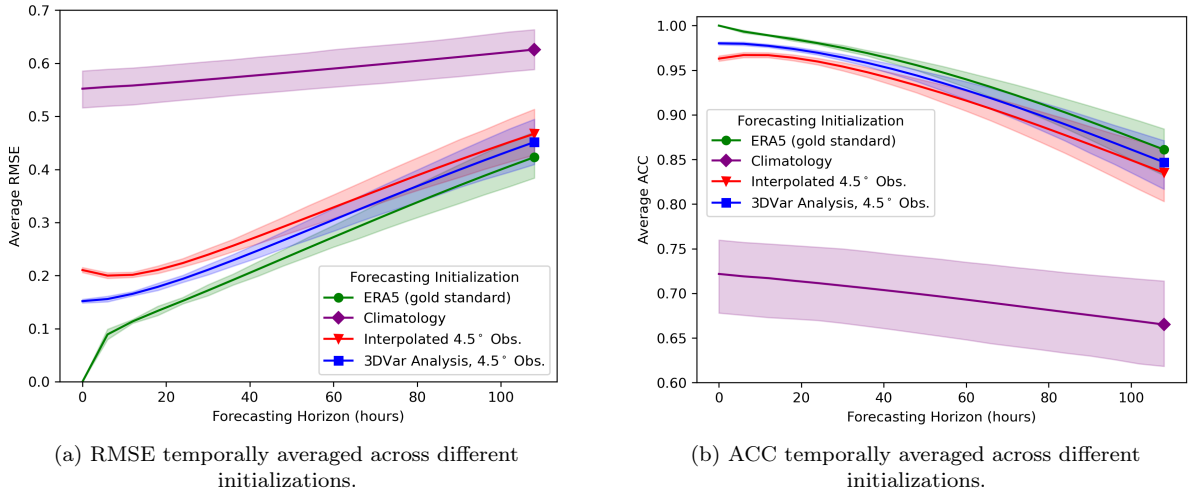


Figure 4: Plots of the 120 hour forecasting performance using (a) interpolated 4.5° observations, (b) ground truth ERA5 data, (c) 3DVar analyses with 4.5° observation resolution, and (d) climatology as initializations. Each line corresponds to the performance at each forecasting horizon in 6 hour increments averaged across different time points for the initial conditions. The shaded regions correspond to the 0.05 and 0.95 quantiles of the forecasting metrics at each forecasting horizon. We also plot the $t = 0$ errors, which corresponds to the initialization error prior to forecasting.

We evaluate forecasts that use three different initializations: (1) our 3DVar analysis with 4.5° observations, (2) interpolated 4.5° observations, and, as an idealized comparison, (3) ground truth ERA5 data. Comparing our 3DVar-initialized forecasts against interpolated-observation-initialized forecasts allows us to assess the gain in performance as a result of our data assimilation framework, and comparing our 3DVar initialized forecasts against ground truth ERA5 initialized forecasts allows us to assess the performance gap in how well our 3DVar forecasts perform compared to how well we could hope to perform in an ideal scenario, where we have access to the full ground truth initial condition.

Forecasting the eye of Typhoon Mawar from May 23, 2023 to May 30, 2023. Our first typhoon forecasting assessment focuses on assessing the predicted location of the eye of the hurricane, which we characterize by the location of the minimum mean sea level pressure.

For each of our initialization types, we add $\mathcal{N}(0, 0.3I_{d_x})$ noise to each standardized initial estimate and create an ensemble of size 50 with these perturbations. Figure 5 visualizes the ensemble of predicted typhoon trajectories for each of our three forecasting initializations. In these plots, we include the ground truth trajectory, labeled as “Ground Truth ERA5,” to evaluate whether this ground truth trajectory is included in the ensemble spread for each initialization type.

While on the tail of the distributions, the ground truth typhoon trajectory is included in the ensemble spread for almost the full trajectory of the typhoon for both the idealized setting (initializing with noisy ground truth ERA5 data) and our setting (initializing with noisy 3DVar analyses using 4.5° observations). On the other hand, initializing with noisy interpolated 4.5° observations appears to forecast an ensemble spread that does not capture the ground truth trajectory as well as our 3DVar analysis initialization or the ground truth ERA5 initialization.

Forecasting the maximum wind speed 10 meters above the surface and minimum mean sea level pressure. Aside from tracking the location of the typhoon, two other important ways to quantitatively characterize the typhoon include assessing the predicted minimum mean sea level pressure and maximum wind speed at 10 meters above the surface. These two features determine the categorization of the typhoon, so in order to accurately predict the intensity of the storm, predictions need to be especially accurate regarding these two features. Because wind speed is not a feature native to ERA5 data, we derived the wind speed 10 above the surface using the formula $\sqrt{U10^2 + V10^2}$, where U10 and V10 correspond to the U- and V- component wind speed at 10m above the surface, respectively. Figure 6 plots forecasts for these two features across the different initializations we consider, initializing on May 23, 2023. These plots include the ground truth ERA5 minimum mean sea level pressure and maximum wind speed 10m above the surface across our forecasting horizon as a visual comparison.

We note that generally, all three of our initializations under-predict the true intensity of the storm; the

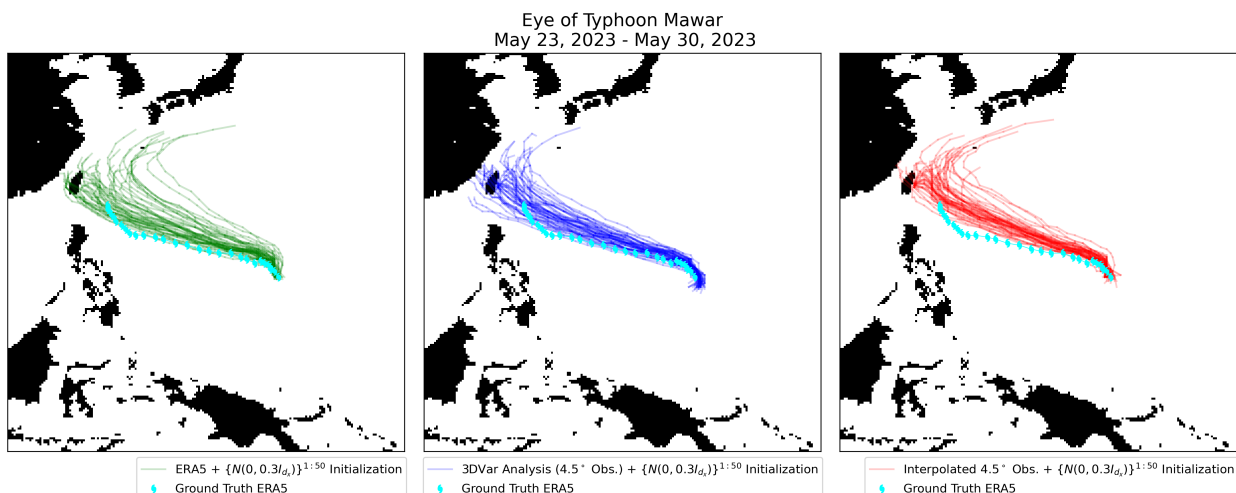
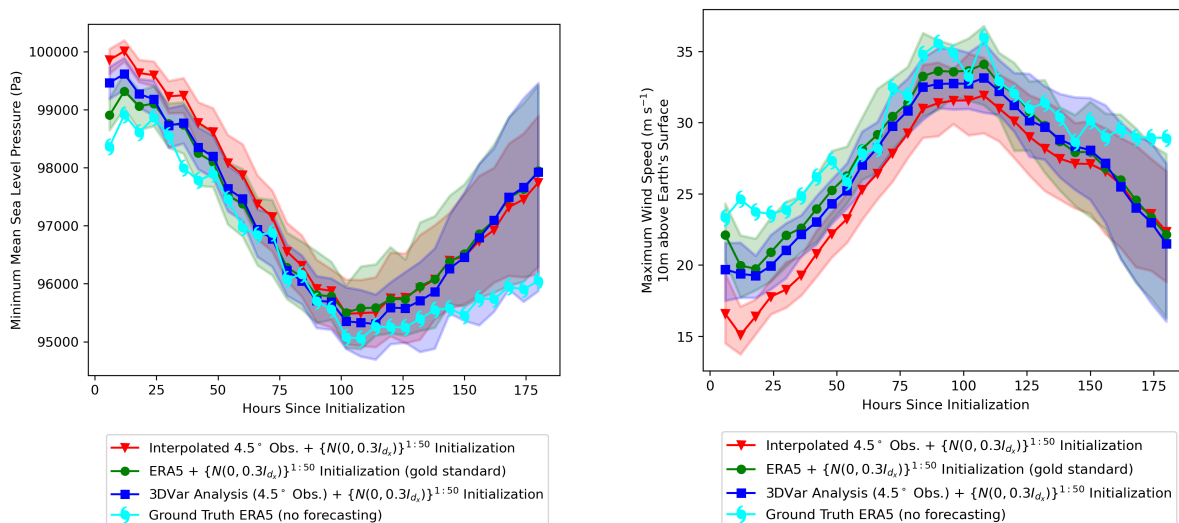


Figure 5: Visualization of the 7 day forecast of the estimated eye of Typhoon Mawar initialized on May 23, 2023 using three different initial conditions: ground truth ERA5 data as a gold standard (left), our 3DVar analysis using 4.5° noisy observations (middle), and interpolated 4.5° noisy observations (right). Each standardized initialization is perturbed by $\mathcal{N}(0, 0.3I_{d_x})$ noise to create a 50 member ensemble. These initial ensemble members were then independently propagated forward in time using FourCastNet without any additional data to correct these forecasts.

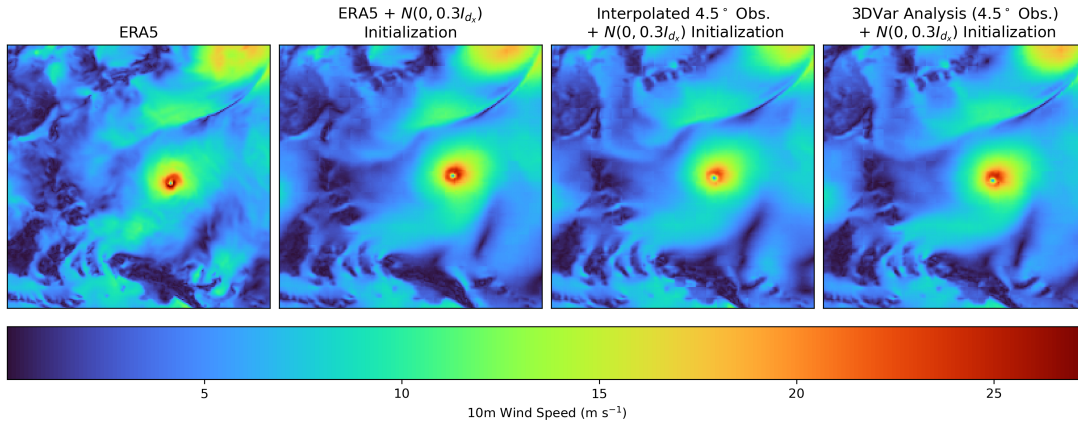


(a) Predicted minimum sea level pressure across different initial conditions compared to the actual minimum sea level pressure.

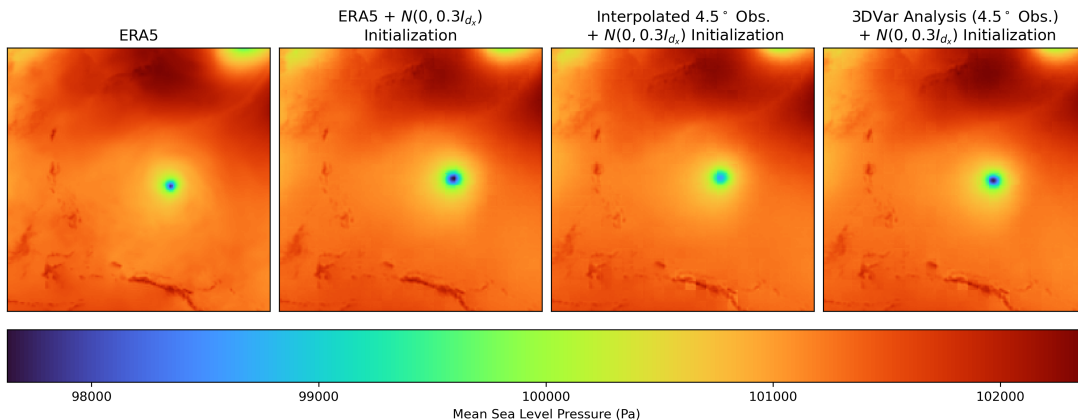
(b) Predicted maximum wind speed at 10 meters above the surface across different initial conditions compared to the actual maximum 10 meter wind speed.

Figure 6: Plots of the forecasted minimum mean sea level pressure and maximum wind speed 10 meters above the surface, initialized with ground truth ERA5 data, interpolated 4.5° observations, and our 3DVar analysis using 4.5° observations on May 23, 2023. The ground truth is additionally plotted to compare these forecasts. For each of our three initial conditions, we create an ensemble of size 50 by adding $\mathcal{N}(0, 0.3I_{d_x})$ distributed noise to the standardized initializations. The forecasts were then converted back to its original scale to produce these plots. The shaded regions in both plots correspond to the 0.05 and the 0.95 quantiles of the ensemble predictions.

predicted minimum mean sea level pressure is larger than ground truth across our forecasting horizon for all three initializations, and the predicted wind speed at 10m above the surface is lower than the ground truth across our forecasting horizon for all three initializations, both of which correspond to predicting a less intense typhoon. However, especially apparent in short forecasts, our 3DVar analysis produces predicted minimum mean sea level pressure and maximum 10m wind speed closer to the “gold standard” forecasts (i.e., initializing with ground truth ERA5 data) and to the actual ground truth compared to the interpolated 4.5° observation forecasts. The smoothed out features in the interpolated 4.5° observations likely further contribute to under-predicting this extreme event. As the forecasting horizon increases, the advantage of our 3DVar analysis initialization appears to lessen after an approximate 2 day forecast horizon, as shown by the vast overlap in the ensemble quantiles.



(a) Ground truth ERA5 (left) and 48 hour forecasted (right-most three) wind speed at 10 meters above the surface on May 25, 2023.



(b) Ground truth ERA5 (left) and 48 hour forecasted (right-most three) mean sea level pressure on May 25, 2023.

Figure 7: Visualization of the ground truth ERA5 wind speed at 10m above the surface and mean sea level pressure compared to 48 hour forecasts given three initial conditions: noisy ERA5 data, noisy interpolated 4.5° observations, and a noisy 3DVar analysis (4.5° observations).

48 hour forecast of Typhoon Mawar, initialized on May 23, 2023. To qualitatively visualize the difference in predictions for our three initial conditions in terms of the wind speed and the sea level pressure, we provide plots of one ensemble member’s 48 hour forecasts in Figures 7a and 7b, corresponding to May 25, 2023, using our three initializations. We include the ground truth for May 25, 2023 in these figures as a visual comparison. Consistent with the conclusion drawn from Figure 6, the 48 hour forecast for interpolated 4.5° observations shows a less extreme forecast in terms of wind speed and mean sea level pressure compared to the ground truth. The forecasts from initializing with the ground truth and a 3DVar analysis (4.5° observations) show a qualitatively better prediction of the eye of the hurricane, more closely matching its intensity. For a more thorough assessment across different ensemble members, we include a comparison of three other ensemble forecasts in Appendix E.

7 Conclusions

We empirically show and theoretically justify that filter stability, particularly using 3DVar, is achievable in settings with surrogate weather dynamics models, which allow for substantial computational speedup compared to filtering with NWP models. We additionally show that forecasting with 3DVar initializations produced from a data-driven weather surrogate can provide more accurate short-term predictions than with more naive approaches to initialization, such as using interpolated observations. We note that results using 3DVar with data-driven weather surrogates can potentially be improved with a more physically-informed choice of background covariance C by providing improved stability.

The success of our filtering experiments in our global setting offers promise to future directions. Specifically, a more challenging yet important future direction is assimilating real observations, which involves data collected irregularly over the globe, and measurements that may not directly correspond to an atmospheric feature in the latent space. In these settings, a nonlinear observation operator is needed to transform the observations from quantities that indirectly measure the feature of interest into that feature. Future research in this direction can assess issues that arise due to non-linearities in the observation process, as well as the impact of associated measurement noise on the long-term filtering stability.

We emphasize that, despite the fact that our observational dataset (1) lies on a regular grid, (2) directly measures the quantities in our latent space, and (3) has low measurement error, our results provide positive implications for the task of assimilating coarse NWP forecasts. Assimilating these coarse forecasts can be done to reduce the cost of expensive NWP solvers while still providing high-resolution, accurate estimates of the latent space. These coarse NWP forecasts can provide important information to assimilate into surrogate models' forecasts, particularly in maintaining longer horizon forecast accuracy, at a cost substantially cheaper than high-resolution NWP solves. Since our results show physically realistic-looking filtering results that have stable errors over a long time horizon, data assimilation with weather surrogates shows substantial promise for applications in this direction.

8 Acknowledgments

MA is grateful to be supported by the National Science Foundation Graduate Research Fellowship under Grant No. DGE-1746045. DSA is grateful for the support of the NSF CAREER award DMS-2237628, DOE DE-SC0022232, and the BBVA Foundation. RW is grateful for the support of NSF DMS-1930049, NSF OAC-1934637, DOE DE-SC0022232, and NSF DMS-2023109. This research used resources of the National Energy Research Scientific Computing Center, a DOE Office of Science User Facility supported by the Office of Science of the U.S. Department of Energy under Contract No. DE-AC02-05CH11231 using NERSC award ASCR-ERCAP0022809.

The authors also thank Mihai Anitescu and Philip Dinenis for helpful discussions regarding our experimental results, and Jaideep Pathak, Morteza Mardani, and Karthik Kashinath for useful insights in the motivation for this work.

References

- K. Bi, L. Xie, H. Zhang, X. Chen, X. Gu, and Q. Tian. Accurate medium-range global weather forecasting with 3D neural networks. *Nature*, 619(7970):533–538, 2023. ISSN 14764687. doi:[10.1038/s41586-023-06185-3](https://doi.org/10.1038/s41586-023-06185-3).
- M. Bocquet. Surrogate modeling for the climate sciences dynamics with machine learning and data assimilation. *Frontiers in Applied Mathematics and Statistics*, 9, 2023. ISSN 2297-4687. doi:[10.3389/fams.2023.1133226](https://doi.org/10.3389/fams.2023.1133226). URL <https://www.frontiersin.org/articles/10.3389/fams.2023.1133226>.
- A. Chattopadhyay, M. Mustafa, P. Hassanzadeh, E. Bach, and K. Kashinath. Towards physics-inspired data-driven weather forecasting: integrating data assimilation with a deep spatial-transformer-based U-NET in a case study with ERA5. *Geoscientific Model Development*, 15(5):2221–2237, 2022. doi:[10.5194/gmd-15-2221-2022](https://doi.org/10.5194/gmd-15-2221-2022). URL <https://gmd.copernicus.org/articles/15/2221/2022/>.
- K. Chen, T. Han, J. Gong, L. Bai, F. Ling, J.-J. Luo, X. Chen, L. Ma, T. Zhang, R. Su, Y. Ci, B. Li, X. Yang, and W. Ouyang. FengWu: Pushing the skillful global medium-range weather forecast beyond 10 days lead, 2023a.
- L. Chen, X. Zhong, F. Zhang, Y. Cheng, Y. Xu, Y. Qi, and H. Li. FuXi: a cascade machine learning forecasting system for 15-day global weather forecast. *npj Climate and Atmospheric Science*, 6(1):1–11, 2023b. ISSN 23973722. doi:[10.1038/s41612-023-00512-1](https://doi.org/10.1038/s41612-023-00512-1).

- M. Chen, S. Mei, J. Fan, and M. Wang. An overview of diffusion models: Applications, guided generation, statistical rates and optimization, 2024. URL <https://arxiv.org/abs/2404.07771v1>.
- N. Chen. Stochastic Methods for Modeling and Predicting Complex Dynamical Systems: Uncertainty Quantification, State Estimation, and Reduced-Order Models. chapter 10, pages 171–177. Springer Charm, 2023. ISBN 978-3-031-22249-8. doi:<https://doi.org/10.1007/978-3-031-22249-8>.
- S. Cheng, C. Quilodrán-Casas, S. Ouala, A. Farchi, C. Liu, P. Tandeo, R. Fablet, D. Lucor, B. Iooss, J. Brajard, D. Xiao, T. Janjic, W. Ding, Y. Guo, A. Carrassi, M. Bocquet, and R. Arcucci. Machine learning with data assimilation and uncertainty quantification for dynamical systems: A review. *IEEE/CAA Journal of Automatica Sinica*, 10(6):1361–1387, 2023. doi:[10.1109/JAS.2023.123537](https://doi.org/10.1109/JAS.2023.123537).
- D. Crisan and B. Rozovskii. *The Oxford Handbook of Nonlinear Filtering*. Oxford University Press, 2011.
- A. Dosovitskiy, L. Beyer, A. Kolesnikov, D. Weissenborn, X. Zhai, T. Unterthiner, M. Dehghani, M. Minderer, G. Heigold, S. Gelly, J. Uszkoreit, and N. Houlsby. An image is worth 16x16 words: Transformers for image recognition at scale. In *International Conference on Learning Representations*, 2021. URL <https://openreview.net/forum?id=YicbFdNTTy>.
- L. S. Gandin. Objective analysis of meteorological fields. Translated from the Russian. Jerusalem (Israel Program for Scientific Translations), 1965. Pp. vi, 242: 53 Figures; 28 Tables. £4 1s. 0d. *Quarterly Journal of the Royal Meteorological Society*, 92(393):447–447, 1966. doi:<https://doi.org/10.1002/qj.49709239320>. URL <https://rmets.onlinelibrary.wiley.com/doi/abs/10.1002/qj.49709239320>.
- J. Guibas, M. Mardani, Z. Li, A. Tao, A. Aanandkumar, and B. Catanzaro. Adaptive fourier neural operators: efficient token mixers for transformers. *ICLR 2022 - 10th International Conference on Learning Representations*, 2022.
- K. Hayden, E. Olson, and E. S. Titi. Discrete data assimilation in the Lorenz and 2D Navier–Stokes equations. *Physica D: Nonlinear Phenomena*, 240(18):1416–1425, 2011.
- H. Hersbach, B. Bell, P. Berrisford, S. Hirahara, A. Horányi, J. Muñoz-Sabater, J. Nicolas, C. Peubey, R. Radu, D. Schepers, A. Simmons, C. Soci, S. Abdalla, X. Abellan, G. Balsamo, P. Bechtold, G. Biavati, J. Bidlot, M. Bonavita, G. De Chiara, P. Dahlgren, D. Dee, M. Diamantakis, R. Dragani, J. Flemming, R. Forbes, M. Fuentes, A. Geer, L. Haimberger, S. Healy, R. J. Hogan, E. Hólm, M. Janisková, S. Keeley, P. Laloyaux, P. Lopez, C. Lupu, G. Radnoti, P. de Rosnay, I. Rozum, F. Vamborg, S. Villaume, and J.-N. Thépaut. The ERA5 global reanalysis. *Quarterly Journal of the Royal Meteorological Society*, 146(730):1999–2049, 2020. doi:<https://doi.org/10.1002/qj.3803>. URL <https://rmets.onlinelibrary.wiley.com/doi/abs/10.1002/qj.3803>.
- H. Hersbach, B. Bell, P. Berrisford, G. Biavati, A. Horányi, J. Muñoz Sabater, J. Nicolas, C. Peubey, R. Radu, I. Rozum, D. Schepers, A. Simmons, C. Soci, D. Dee, and J.-N. Thépaut. Era5-land hourly data from 1950 to present. Copernicus Climate Change Service (C3S) Climate Data Store (CDS), 2023. Accessed on 03 March 2024.
- L. Huang, L. Gianinazzi, Y. Yu, P. D. Dueben, and T. Hoefler. DiffDA: a diffusion model for weather-scale data assimilation, 2024. URL <http://arxiv.org/abs/2401.05932>.
- R. E. Kalman. A new approach to linear filtering and prediction problems. *Journal of Basic Engineering*, 82(1): 35–45, 03 1960. ISSN 0021-9223. doi:[10.1115/1.3662552](https://doi.org/10.1115/1.3662552). URL <https://doi.org/10.1115/1.3662552>.
- E. Kalnay. *Atmospheric Modeling, Data Assimilation and Predictability*. Cambridge University Press, 2003.
- R. Keisler. Forecasting global weather with graph neural networks, 2022. URL <https://arxiv.org/abs/2202.07575>.
- V. Krasnopolsky. Review: using machine learning for data assimilation, model physics, and post-processing model outputs. Technical Report April, Environmental Modeling Center (U.S.); National Centers for Environmental Prediction (U.S.), 2023. URL <https://repository.library.noaa.gov/view/noaa/50158>.
- R. Lam, A. Sanchez-Gonzalez, M. Willson, P. Wirnsberger, M. Fortunato, F. Alet, S. Ravuri, T. Ewalds, Z. Eaton-Rosen, W. Hu, A. Merose, S. Hoyer, G. Holland, O. Vinyals, J. Stott, A. Pritzel, S. Mohamed, and P. Battaglia. Learning skillful medium-range global weather forecasting. *Science*, 382(6677):1416–1421, 2023. doi:[10.1126/science.adi2336](https://doi.org/10.1126/science.adi2336). URL <https://www.science.org/doi/abs/10.1126/science.adi2336>.
- K. J. Law, D. Sanz-Alonso, A. Shukla, and A. M. Stuart. Filter accuracy for the Lorenz 96 model: Fixed versus adaptive observation operators. *Physica D: Nonlinear Phenomena*, 325:1–13, 2016.

- F.-X. Le Dimet and A. Nouailler. Assimilation of dynamical data in a limited area model. In Y. K. SASAKI, editor, *Variational Methods in Geosciences*, volume 5 of *Developments in Geomathematics*, pages 181–185. Elsevier, 1986. doi:<https://doi.org/10.1016/B978-0-444-42697-0.50030-8>. URL <https://www.sciencedirect.com/science/article/pii/B9780444426970500308>.
- A. C. Lorenc, S. P. Ballard, R. S. Bell, N. B. Ingleby, P. L. F. Andrews, D. M. Barker, J. R. Bray, A. M. Clayton, T. Dalby, D. Li, T. J. Payne, and F. W. Saunders. The Met. Office global three-dimensional variational data assimilation scheme. *Quarterly Journal of the Royal Meteorological Society*, 126(570):2991–3012, 2000. doi:<https://doi.org/10.1002/qj.49712657002>. URL <https://rmets.onlinelibrary.wiley.com/doi/abs/10.1002/qj.49712657002>.
- R. Maulik, V. Rao, J. Wang, G. Mengaldo, E. Constantinescu, B. Lusch, P. Balaprakash, I. Foster, and R. Kotamarthi. Efficient high-dimensional variational data assimilation with machine-learned reduced-order models. *Geoscientific Model Development*, 15(8):3433–3445, 2022. doi:[10.5194/gmd-15-3433-2022](https://doi.org/10.5194/gmd-15-3433-2022). URL <https://gmd.copernicus.org/articles/15/3433/2022/>.
- A. J. F. Moodey, A. S. Lawless, R. W. E. Potthast, and P. J. van Leeuwen. Nonlinear error dynamics for cycled data assimilation methods. *Inverse Problems*, 29(2):025002, jan 2013. doi:[10.1088/0266-5611/29/2/025002](https://doi.org/10.1088/0266-5611/29/2/025002). URL <https://dx.doi.org/10.1088/0266-5611/29/2/025002>.
- National Environmental Satellite, Data, and Information Service, NOAA. Typhoon Mawar Barrels Across the North Pacific. <https://www.nesdis.noaa.gov/news/typhoon-mawar-barrels-across-the-north-pacific>, 2023. Accessed: 2024-04-20.
- D. F. Parrish and J. C. Derber. The national meteorological center’s spectral statistical-interpolation analysis system. *Monthly Weather Review*, 120(8):1747 – 1763, 1992. doi:[10.1175/1520-0493\(1992\)120<1747:TNMCSS>2.0.CO;2](https://doi.org/10.1175/1520-0493(1992)120<1747:TNMCSS>2.0.CO;2). URL https://journals.ametsoc.org/view/journals/mwre/120/8/1520-0493_1992_120_1747_tnmcss_2_0_co_2.xml.
- J. Pathak, S. Subramanian, P. Harrington, S. Raja, A. Chattopadhyay, M. Mardani, T. Kurth, D. Hall, Z. Li, K. Azizzadenesheli, P. Hassanzadeh, K. Kashinath, and A. Anandkumar. FourCastNet: a global data-driven high-resolution weather model using adaptive Fourier neural operators, 2022. URL <http://arxiv.org/abs/2202.11214>.
- L. M. Pecora and T. L. Carroll. Synchronization in chaotic systems. *Physical Review Letters*, 64(8):821, 1990.
- S. Rasp, P. D. Dueben, S. Scher, J. A. Weyn, S. Mouatadid, and N. Thuerey. Weatherbench: A benchmark data set for data-driven weather forecasting. *Journal of Advances in Modeling Earth Systems*, 12(11):e2020MS002203, 2020. doi:<https://doi.org/10.1029/2020MS002203>. URL <https://agupubs.onlinelibrary.wiley.com/doi/abs/10.1029/2020MS002203>. e2020MS002203 10.1029/2020MS002203.
- F. Rawlins, S. P. Ballard, K. J. Bovis, A. M. Clayton, D. Li, G. W. Inverarity, A. C. Lorenc, and T. J. Payne. The Met Office global four-dimensional variational data assimilation scheme. *Quarterly Journal of the Royal Meteorological Society*, 133(623):347–362, 2007. doi:<https://doi.org/10.1002/qj.32>. URL <https://rmets.onlinelibrary.wiley.com/doi/abs/10.1002/qj.32>.
- L. F. Richardson. *Weather Prediction by Numerical Process*. Cambridge University Press, 1922.
- J. M. Sabater. ERA5-Land hourly data from 1950 to present. Copernicus Climate Change Service (C3S) Climate Data Store (CDS), 2019. Accessed on 05 March 2024.
- D. Sanz-Alonso and A. M. Stuart. Long-time asymptotics of the filtering distribution for partially observed chaotic dynamical systems. *SIAM/ASA Journal on Uncertainty Quantification*, 3(1):1200–1220, 2015.
- D. Sanz-Alonso, A. Stuart, and A. Taeb. *Inverse Problems and Data Assimilation*, volume 107. Cambridge University Press, 2023.
- Y. Tang, Z. Deng, K. K. Manoj, and D. Chen. A practical scheme of the sigma-point kalman filter for high-dimensional systems. *Journal of Advances in Modeling Earth Systems*, 6(1):21–37, 2014. doi:<https://doi.org/10.1002/2013MS000255>. URL <https://agupubs.onlinelibrary.wiley.com/doi/abs/10.1002/2013MS000255>.
- The President’s Council of Advisors on Science and Technology. REPORT TO THE PRESIDENT Supercharging Research: Harnessing Artificial Intelligence to Meet Global Challenges. Technical report, Executive Office of the President, The White House, Washington, D.C., 2024. URL https://www.whitehouse.gov/wp-content/uploads/2024/04/AI-Report_Upload_29APRIL2024_SEND-2.pdf.

J. Tollefson. Climate scientists push for access to world’s biggest supercomputers to build better Earth models. *Springer Nature*, jul 2023. doi:<https://doi.org/10.1038/d41586-023-02249-6>. URL <https://www.nature.com/articles/d41586-023-02249-6#:~:text=11July2023-,Climatescientistspushforaccesstoworld’sbiggestsupercomputersto,theeffectsofglobalwarming.&text=HowquicklywillEarthwarm,thatmeanfortheplanet%3F>.

Y. Xiao, L. Bai, W. Xue, K. Chen, T. Han, and W. Ouyang. FengWu-4DVar: Coupling the data-driven weather forecasting model with 4D variational assimilation, 2023. URL <https://arxiv.org/abs/2312.12455>.

A Visualization of ground truth ERA5 and 4.5 degrees ERA5 observations for relative humidity at 500 hPa.

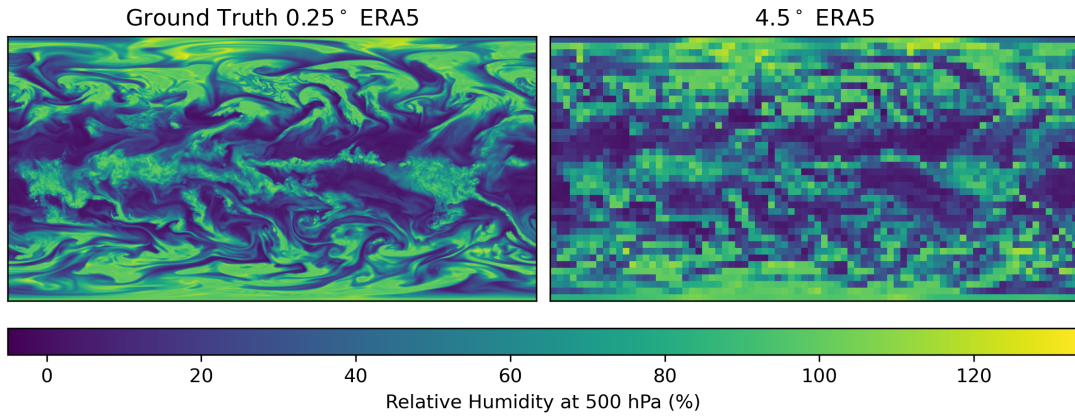


Figure 8: Visual comparison of 0.25° ERA5 data and our 4.5° observations created by systematically thinning out the 0.25° ERA5 data. This plot corresponds to December 31, 2023 at 18:00 UTC.

Figure 8 provides a visual comparison of one time point of relative humidity at 500 hPa for 0.25° ERA5 compared to ERA5 data thinned out to a resolution of 4.5°. In plotting the 4.5° observations, we mapped this data up to a 720×1440 grid via nearest neighbors, resulting in a pixelated-looking image.

B Proof of Theorem 1

This appendix contains the proof of Theorem 1. The proof follows closely those of Theorem 3.2 in Moodey et al. [2013] and Theorem 9.2 in Sanz-Alonso et al. [2023].

Proof. Throughout the proof, c will denote a constant that may change from line-to-line. First, we introduce x_t^o as the “operational” 3DVar analysis using observations y_t and the “true” dynamics map \mathcal{F} . Specifically, for $t = 0$ we set $x_0^o = x_0^s$, and then we recursively define

$$x_t^o = (I - KH)\mathcal{F}(x_{t-1}^o) + Ky_t, \quad t \geq 1. \quad (10)$$

In operational weather settings, \mathcal{F} is a NWP model.

The main idea of this proof is to decompose the error $\|x_t^s - x_t^{\text{true}}\|$ into two components:

- (a) filtering error with 3DVar using the true dynamics \mathcal{F} ; and
- (b) the distance between analyses from 3DVar using the true dynamics \mathcal{F} and 3DVar using the surrogate dynamics \mathcal{F}_s .

This decomposition can formally be written as

$$\|x_t^s - x_t^{\text{true}}\| \leq \underbrace{\|x_t^o - x_t^{\text{true}}\|}_{(a)} + \underbrace{\|x_t^s - x_t^o\|}_{(b)}. \quad (11)$$

(a) **Filtering error with 3DVar using the true dynamics \mathcal{F} .**

First focusing on term (a) in inequality (11), we can rewrite x_t^{true} and x_t^o as

$$x_t^{\text{true}} = (I - KH)\mathcal{F}(x_{t-1}^{\text{true}}) + KH\mathcal{F}(x_{t-1}^{\text{true}}) \quad (12)$$

$$x_t^o = (I - KH)\mathcal{F}(x_{t-1}^o) + \underbrace{KH\mathcal{F}(x_{t-1}^{\text{true}})}_{=KH\mathcal{F}(x_{t-1}^o)} + \gamma K\eta_t, \quad (13)$$

where we use Assumption 1 to write $KH\mathcal{F}(x_{t-1}^o) = KH\mathcal{F}(x_{t-1}^{\text{true}}) + \gamma K\eta_t$. Subtracting (12) from (13), we obtain

$$\begin{aligned} x_t^o - x_t^{\text{true}} &= (I - KH) [\mathcal{F}(x_{t-1}^o) - \mathcal{F}(x_{t-1}^{\text{true}})] + \gamma K\eta_t \\ &= \left[\int_0^1 (I - KH) D\mathcal{F}(zx_{t-1}^o + (1-z)x_{t-1}^{\text{true}}) dz \right] (x_{t-1}^o - x_{t-1}^{\text{true}}) + \gamma K\eta_t, \end{aligned}$$

where we apply the mean-value-theorem for vector-valued functions to the first term. We then take the norm of both sides of the inequality

$$\begin{aligned} \|x_t^o - x_t^{\text{true}}\| &\leq \left[\int_0^1 \|(I - KH) D\mathcal{F}(zx_{t-1}^o + (1-z)x_{t-1}^{\text{true}})\| dz \right] \|x_{t-1}^o - x_{t-1}^{\text{true}}\| + \gamma \|K\eta_t\| \\ &\leq \lambda \|x_{t-1}^o - x_{t-1}^{\text{true}}\| + \gamma \|K\eta_t\|, \end{aligned}$$

where we use the assumption in inequality (7) in Theorem 1. By further taking the expectation of both sides of the inequality,

$$\mathbb{E}\|x_t^o - x_t^{\text{true}}\| \leq \lambda \mathbb{E}\|x_{t-1}^o - x_{t-1}^{\text{true}}\| + c\gamma,$$

where we assume that the scaled measurement noise $\|K\eta_t\|$ is bounded above by some constant $c > 0$. Therefore, we recursively deduce that

$$\begin{aligned} \mathbb{E}\|x_t^o - x_t^{\text{true}}\| &\leq \lambda \left(\lambda \mathbb{E}\|x_{t-2}^o - x_{t-2}^{\text{true}}\| + c\gamma \right) + c\gamma \\ &= \lambda^2 \mathbb{E}\|x_{t-2}^o - x_{t-2}^{\text{true}}\| + c\gamma\lambda + c\gamma \leq \dots \leq \lambda^t \mathbb{E}\|x_0^o - x_0^{\text{true}}\| + c\gamma \sum_{i=0}^{t-1} \lambda^i. \end{aligned}$$

Finally, since $\lambda \in (0, 1)$, we conclude that

$$\limsup_{t \rightarrow \infty} \mathbb{E}\|x_t^o - x_t^{\text{true}}\| \leq \frac{\gamma c}{1 - \lambda}. \quad (14)$$

(b) **Distance between analyses from 3DVar using the true dynamics \mathcal{F} and analyses from 3DVar using the surrogate dynamics \mathcal{F}_s .**

Now, shifting focus to finding an upper-bound of term (b) in inequality (11), we can similarly rewrite x_t^s and x_t^o as

$$\begin{aligned} x_t^s &= (I - KH)\mathcal{F}_s(x_{t-1}^s) + \underbrace{KH\mathcal{F}_s(x_{t-1}^{\text{true}})}_{=KH\mathcal{F}_s(x_{t-1}^s)} + \gamma K\eta_t \\ x_t^o &= (I - KH)\mathcal{F}(x_{t-1}^o) + \underbrace{KH\mathcal{F}(x_{t-1}^{\text{true}})}_{=KH\mathcal{F}(x_{t-1}^o)} + \gamma K\eta_t, \end{aligned}$$

where we again use Assumption 1. By writing out the expression for the distance between the analyses from 3DVar using the surrogate dynamics \mathcal{F}_s and from 3DVar using the true dynamics \mathcal{F} , we obtain the following expression

$$\begin{aligned} x_t^s - x_t^o &= (I - KH) [\mathcal{F}_s(x_{t-1}^s) - \mathcal{F}(x_{t-1}^o)] \\ &= (I - KH) [\mathcal{F}_s(x_{t-1}^s) - \mathcal{F}(x_{t-1}^s)] + (I - KH) [\mathcal{F}(x_{t-1}^s) - \mathcal{F}(x_{t-1}^o)] \\ &\leq \varepsilon + \left[\int_0^1 (I - KH) D\mathcal{F}(zx_{t-1}^s + (1-z)x_{t-1}^o) dz \right] (x_{t-1}^s - x_{t-1}^o), \end{aligned}$$

where we utilize the assumption in (8) to upper-bound the first term and the mean-value-theorem for vector-valued functions to rewrite the second term. Taking the norm of both sides gives

$$\begin{aligned} \|x_t^s - x_t^o\| &\leq \varepsilon + \left[\int_0^1 \|(I - KH) D\mathcal{F}(zx_{t-1}^s + (1-z)x_{t-1}^o)\| dz \right] \|x_{t-1}^s - x_{t-1}^o\| \\ &\leq \varepsilon + \lambda \|x_{t-1}^s - x_{t-1}^o\|, \end{aligned}$$

where we again use the assumption of inequality (7) in Theorem 1. By taking the expectation of both sides of the inequality, we obtain the inequality

$$\mathbb{E}\|x_t^s - x_t^o\| \leq \varepsilon + \lambda \mathbb{E}\|x_{t-1}^s - x_{t-1}^o\|.$$

Therefore, by the same recursive argument used to bound term (a), we deduce that

$$\limsup_{t \rightarrow \infty} \mathbb{E}\|x_t^s - x_t^o\| \leq \frac{\varepsilon}{1 - \lambda}. \quad (15)$$

Combining the upper-bounds for (a) and (b) in inequality (11).

By combining the two upper-bounds from (14) and (15), we have the final result

$$\limsup_{t \rightarrow \infty} \mathbb{E}\|x_{t-1}^s - x_t^{\text{true}}\| \leq c \left(\frac{\gamma + \varepsilon}{1 - \lambda} \right).$$

□

C Evaluation metrics

Our results primarily evaluate our results on two metrics: latitude-weighted root mean square error (RMSE) and latitude-weighted anomaly correlation coefficient (ACC). We use these two metrics based on the analysis done in Pathak et al. [2022], which utilized these metrics defined in Rasp et al. [2020].

The latitude-weighted root-mean-square-error (RMSE) at time t across f different features is defined in equation (16) as

$$\text{RMSE}_t = \frac{1}{f} \sum_{f'=1}^f \sqrt{\frac{1}{N_{\text{lat}} N_{\text{lon}}} \sum_{i=1}^{N_{\text{lon}}} \sum_{j=1}^{N_{\text{lat}}} L(j) (\{x_t^s\}_{f',i,j} - \{x_t^{\text{true}}\}_{f',i,j})^2}, \quad (16)$$

where N_{lat} is the number of latitudes, N_{lon} is the number of longitudes, and $L(j)$ is the latitude weighting factor for the j th latitude index, defined in equation (17) as

$$L(j) = \frac{\cos(\text{lat}(j))}{\frac{1}{N_{\text{lat}}} \sum_{j=1}^{N_{\text{lat}}} \cos(\text{lat}(j))}. \quad (17)$$

We additionally utilize the latitude-weighted anomaly correlation coefficient (ACC) at time t across f different features, defined in equation (18) as

$$\text{ACC}_t = \frac{1}{f} \sum_{f'=1}^f \frac{\sum_{i=1}^{N_{\text{lon}}} \sum_{j=1}^{N_{\text{lat}}} L(j) \{x_t^s\}_{f',i,j} \{x_t^{\text{true}}\}_{f',i,j}}{\sqrt{\sum_{i=1}^{N_{\text{lon}}} \sum_{j=1}^{N_{\text{lat}}} (\{x_t^s\}_{f',i,j})^2 \sum_{i=1}^{N_{\text{lon}}} \sum_{j=1}^{N_{\text{lat}}} L(j) (\{x_t^{\text{true}}\}_{f',i,j})^2}} \quad (18)$$

In both equations (16) and (18), $\{x_t^s\}_{f',i,j}$ is defined as an estimate, either through forecasting or filtering, of $\{x_t^{\text{true}}\}_{f',i,j}$ for feature f' at latitude j and longitude i , and $\{x_t^{\text{true}}\}_{f',i,j}$ is the ground truth ERA5 data for feature f' at latitude j and longitude i . In all of our experiments, $N_{\text{lat}} = 720$ and $N_{\text{lon}} = 1440$.

D Assimilation visualizations for all atmospheric features

Figures 9 and 10 visualize the ground truth ERA5 data, interpolated 4.5° noisy observations, and 3DVar analyses using these 4.5° observations for all 20 atmospheric features. The 3DVar analyses were constructed from 365 days of assimilating sparse, noisy 4.5° resolution observations every 6 hours.

The rows of Figure 9 visualize, in order, U-component wind speed at 10 meters above the surface, V-component wind speed at 10 meters above the surface, temperature at 2 meters above the surface, surface pressure, mean sea level pressure, temperature at pressure level 850 hPa, U-component wind speed at pressure level 1000 hPa, V-component wind speed at pressure level 1000 hPa, geopotential at pressure level 1000 hPa, and U-component wind speed at pressure level 850 hPa.

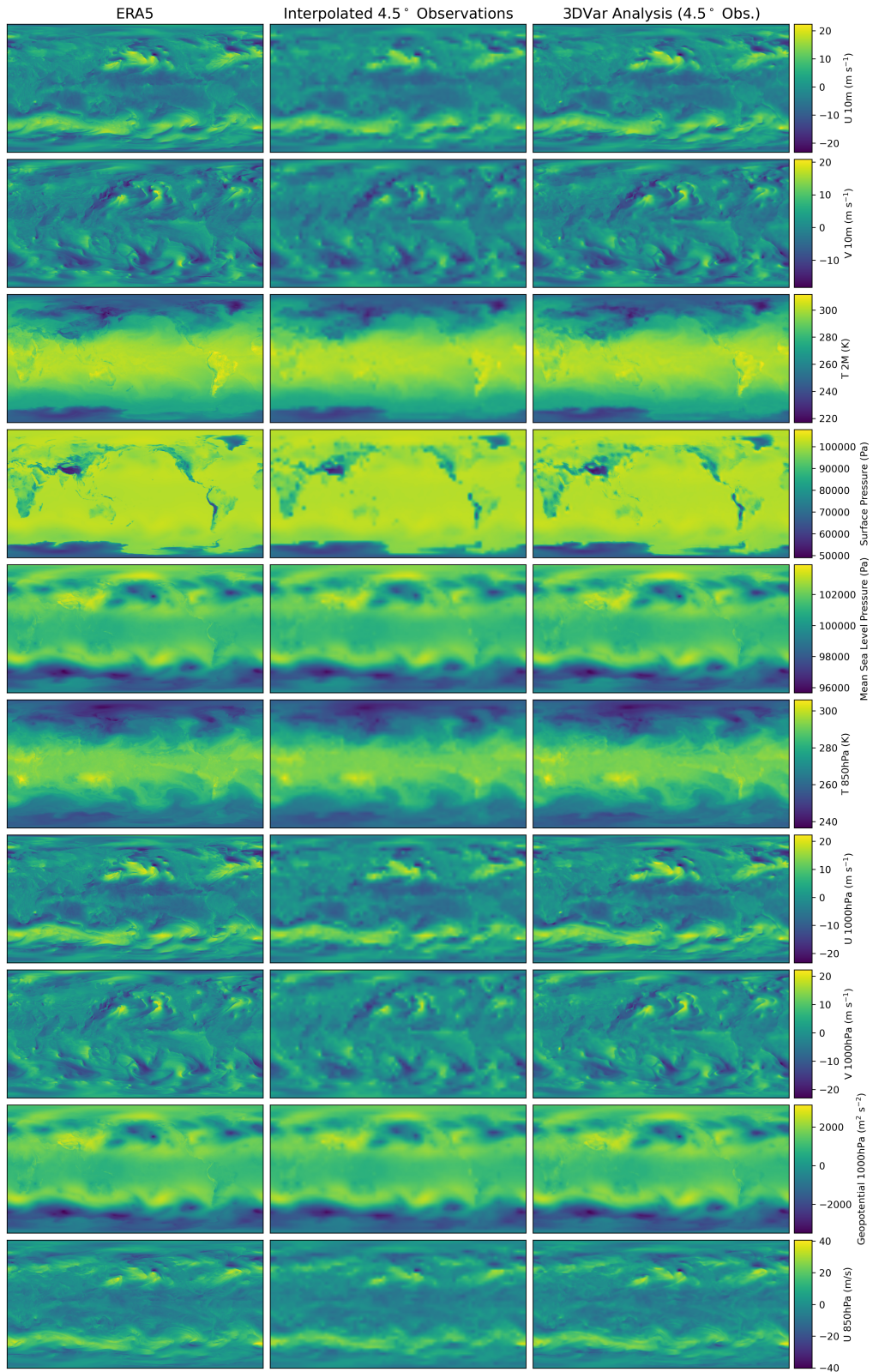


Figure 9: Visualization of the ground truth ERA5 data, interpolated 4.5° ERA5 observations with standardized $N(0, 0.0001I_{d_y})$ distributed additive errors, and our 3DVar analysis using this observational data and FourCastNet for 10 different atmospheric features at the end of our assimilation horizon, December 31, 2023 at 18:00 UTC.

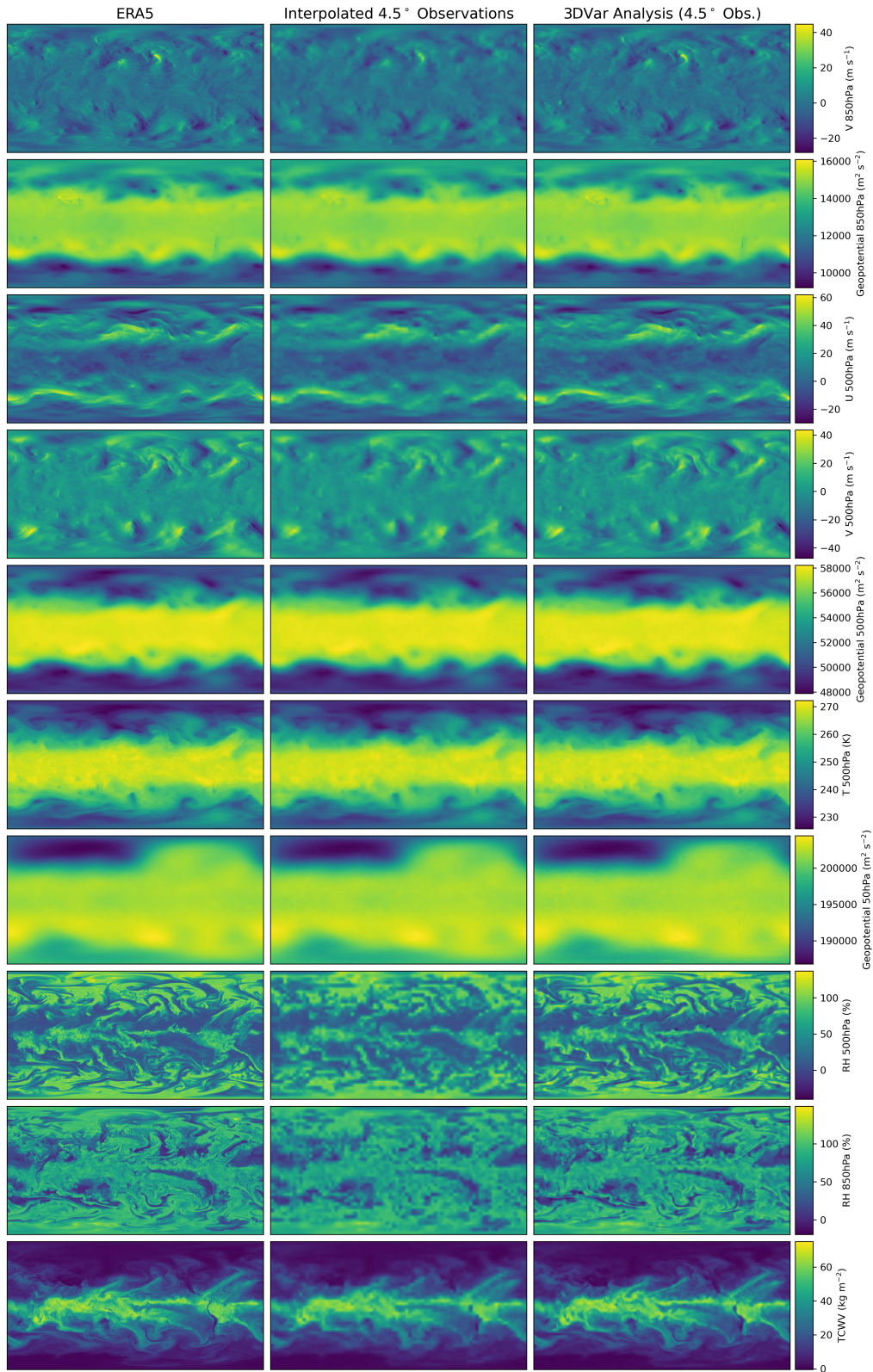


Figure 10: Visualization of the ground truth ERA5 data, interpolated 4.5° ERA5 observations with standardized $N(0, 0.0001I_{d_y})$ distributed additive errors, and our 3DVar analysis using this observational data and FourCastNet for 10 different atmospheric features at the end of our assimilation horizon, December 31, 2023 at 18:00 UTC.

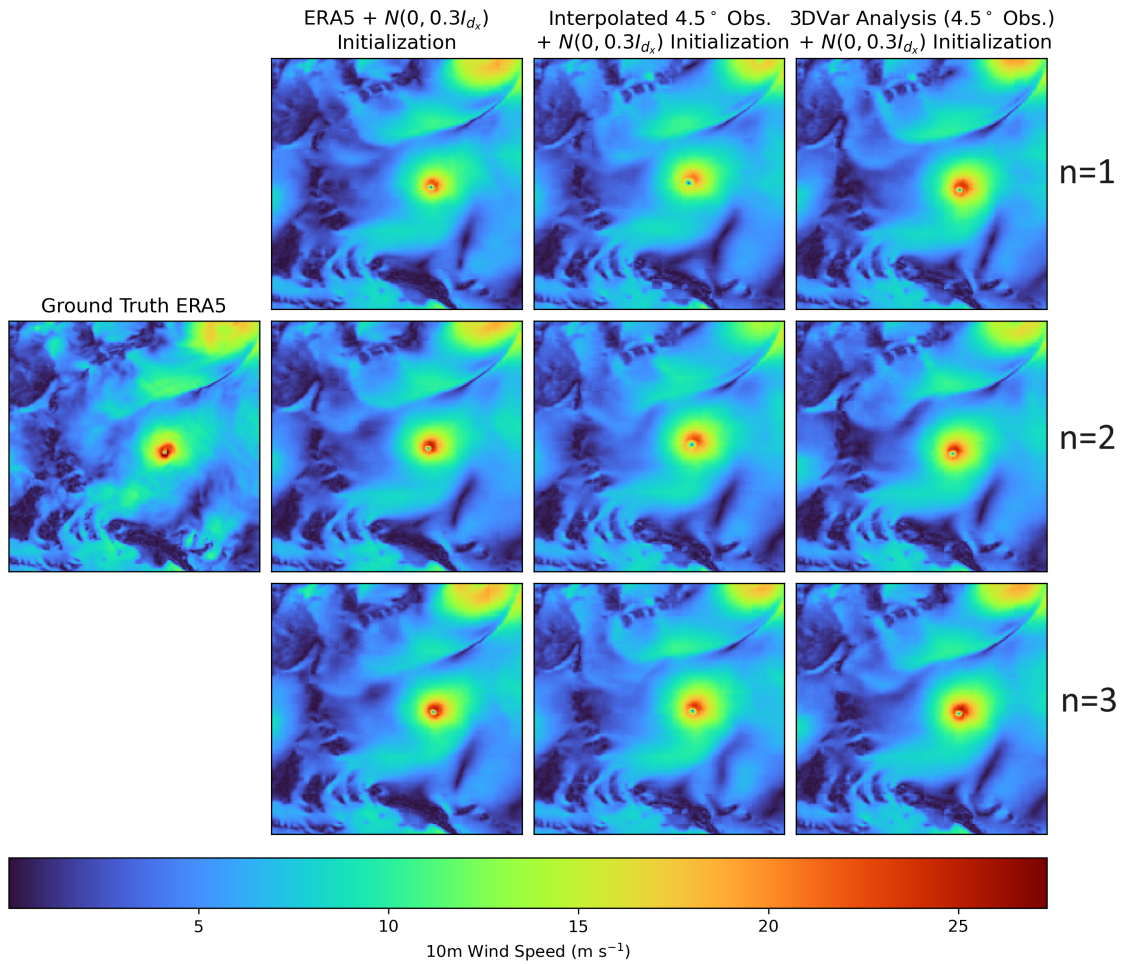


Figure 11: Visualization of three ensemble members' 48 hour forecasts of 10m wind speed for May 25, 2023 using three different initializations: noisy ground truth ERA5 data, noisy interpolated 4.5° observations, and a 3DVar analysis (4.5° observations). For visual reference, we include ground truth ERA5 10m wind speed on May 25, 2023.

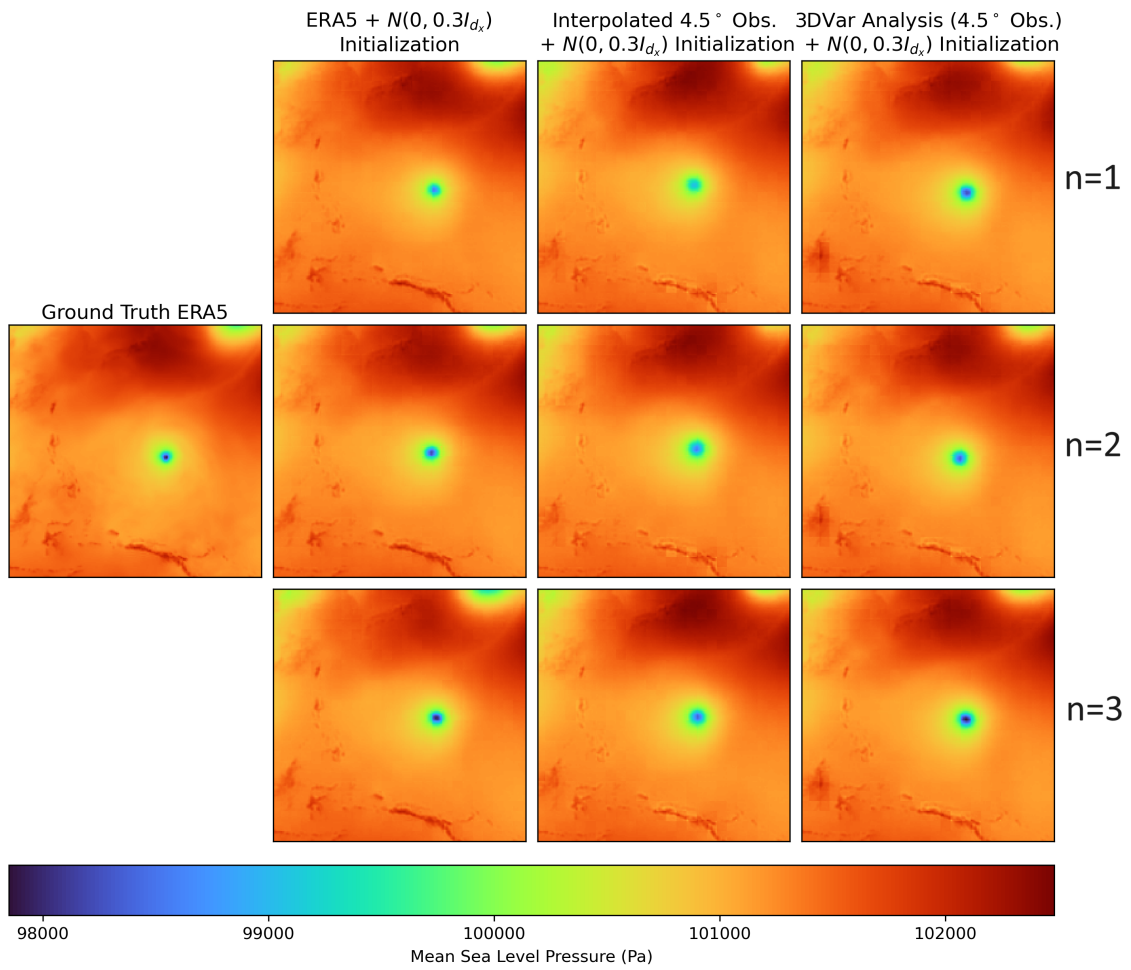


Figure 12: Visualization of three ensemble members' 48 hour forecasts of mean sea level pressure for May 25, 2023 using three different initializations: noisy ground truth ERA5 data, noisy interpolated 4.5° observations, and a 3DVar analysis (4.5° observations). For visual reference, we include ground truth ERA5 10m wind speed on May 25, 2023.

The rows of Figure 10 visualize, in order, V-component wind speed at pressure level 850 hPa, geopotential at pressure level 850 hPa, U-component wind speed at pressure level 500 hPa, V-component wind speed at pressure level 500 hPa, geopotential at pressure level 500 hPa, temperature at pressure level 500 hPa, geopotential at pressure level 50 hPa, relative humidity at at pressure level 500 hPa, relative humidity at pressure level 850 hPa, and total column water vapor.

E Sample 48 hour ensemble forecasts for Typhoon Mawar, 2023

To supplement the single ensemble member visualizations in Figures 7a and 7b, we include visualizations for the 48 hour forecasts of three other randomly selected ensemble members for each of our initial conditions in Figures 11 and 12. As mentioned in the main text, the forecasts from the interpolated 4.5° observations generally tend to result in less extreme predictions compared to the ground truth or the forecasts from initializing with noisy ground truth ERA5 data or our 3DVar analysis (4.5° observations).